Joule

CellPress

Article

High-rate, high-capacity electrochemical energy storage in hydrogen-bonded fused aromatics

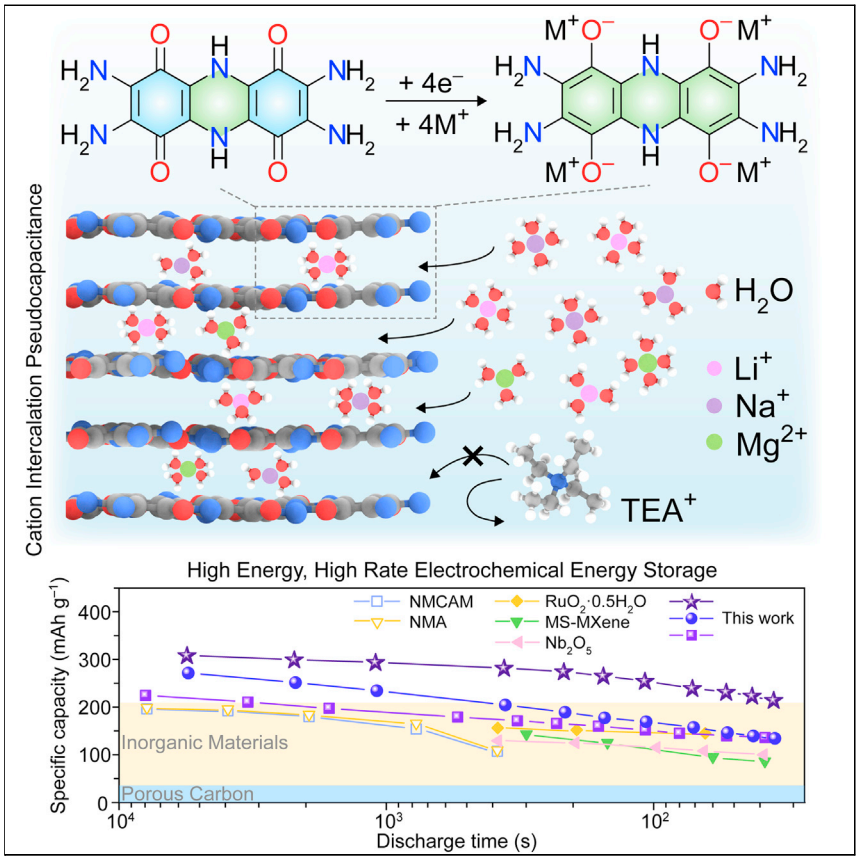

Shortening the charging time for electrochemical energy storage devices, while maintaining their storage capacities, is a major scientific and technological challenge in broader market adoption of such devices. Fused aromatic molecules with abundant redox-active heteroatoms, extended conjugation, and intermolecular hydrogen bonding serve as electrode materials that enable high-rate, high-capacity charge storage. The structural and compositional principles underlining their electrochemical performance provide important blueprints toward the use of organic pseudocapacitive materials in practical, high-rate, high-capacity electrochemical energy storage devices.

Tianyang Chen, Harish Banda, Luming Yang, Jian Li, Yugang Zhang, Riccardo Parenti, Mircea Dincă

mdinca@mit.edu

Highlights

Fused aromatic molecules with abundant heteroatoms are developed for energy storage

Extended conjugation and hydrogen bonding enable rapid conduction of charges

pH-dependent pseudocapacitive intercalation charge storage is realized

A rare combination of high-capacity, high-rate charge storage is achieved

Chen et al., Joule 7, 1–17
May 17, 2023
https://doi.org/10.1016/j.joule.2023.03.011

Please cite this article in press as: Chen et al., High-rate, high-capacity electrochemical energy storage in hydrogen-bonded fused aromatics, Joule (2023), https://doi.org/10.1016/j.joule.2023.03.011

Joule

CellPress

Article

High-rate, high-capacity electrochemical energy storage in hydrogen-bonded fused aromatics

Tianyang Chen,[1,6] Harish Banda,[1,6] Luming Yang,[1] Jian Li,[2,3] Yugang Zhang,[4] Riccardo Parenti,[5] and Mircea Dincă[1,7,*]

SUMMARY

Designing materials for electrochemical energy storage with short charging times and high charge capacities is a longstanding challenge. The fundamental difficulty lies in incorporating a high density of redox couples into a stable material that can efficiently conduct both ions and electrons. We report all-organic, fused aromatic materials that store up to 310 mAh g^{-1} and charge in as little as 33 s. This performance stems from abundant quinone/imine functionalities that decorate an extended aromatic backbone, act as redox-active sites, engage in hydrogen bonding, and enable a delocalized high-rate energy storage with stability upon cycling. The extended conjugation and hydrogen-bonding-assisted bulk charge storage contrast with the surface-confined or hydration-dependent behavior of traditional inorganic electrodes.

INTRODUCTION

Growing demand for electrifying the transportation sector and decarbonizing the grid requires the development of electrochemical energy storage (EES) systems that cater to various energy and power needs.[1,2] As the dominant EES devices, lithium-ion cells (LICs) and electrochemical capacitors typically only offer either high energy or high power.[3] Over the past decade, several attempts were made to achieve high power and energy densities in hybrid energy storage systems by integrating LICs and capacitors at the device level.[4] This approach represents a modular way of supplying high energy and high power to applications where power demands vary with time or the possibility to recover energy at high power is as important as power delivery itself. However, the complexity and costs involved in device-level engineering diminish the utility of hybrid energy storage systems in compact applications such as electric vehicles. This creates a strong incentive to develop electrode materials that combine the high charge capacity of LICs with the fast charging and long cycling life of capacitors.

The combination of high capacity and high power in a single electrode material mandates that the material possesses abundant redox-active sites and that it promotes rapid transport of electrical and ionic charges throughout the electrode bulk. This charge storage mechanism, commonly known as pseudocapacitance, has primarily been identified in redox-active transition metal oxides/nitrides/carbides, which exhibit short charge diffusion lengths when fabricated as thin films.[5] However, when film thickness increases with these materials, as required for practically relevant mass loadings, ion and electron transports dramatically decrease, leading to sub-optimal performance.[6] Overcoming this challenge typically requires composite synthesis[7] and nano-engineering.[8]

CONTEXT & SCALE

Materials with high capacity for electrical energy storage, such as the electrode materials in Li-ion batteries, typically need several hours for a full charge. Conversely, carbonaceous electrodes in electrochemical capacitors charge in a few seconds but store only a fraction of the energy in their batteries. Combining the merits of both devices into a single high-energy, high-power device represents a major scientific and technological challenge. From a design perspective, the difficulty lies in designing electrode materials with a high density of redox sites and excellent charge conduction pathways. Here, we show that heteroatoms on fused aromatic molecules serve as multifunctional sites in enabling high-rate, high-capacity charge storage. Heteroatoms serve as redox-active sites that engage in hydrogen bonding and induce electron delocalization for excellent conduction of ions and electrons. These principles provide avenues for the development of high-energy, high-power storage devices.

Please cite this article in press as: Chen et al., High-rate, high-capacity electrochemical energy storage in hydrogen-bonded fused aromatics, Joule (2023), https://doi.org/10.1016/j.joule.2023.03.011

Organic materials offer an alternative, more compositionally diverse materials space for designing pseudocapacitive electrodes from earth-abundant elements. However, they typically suffer from poor intrinsic electrical conductivity, a result of limited electronic delocalization and high solubility in electrolytes, which leads to poor cyclability. These combine to deliver inferior electrochemical performance compared with the inorganic alternatives.[9] Although strategies such as polymerization and compositing organic molecules with insoluble admixers can limit electrode dissolution, designing organic materials that are themselves insoluble but still allow swift charge transport and storage is difficult.[10] Here, we report bis-tetraaminobenzoquinone (BTABQ) and its polymeric analog poly(bis-tetraaminobenzoquinone) (pBTABQ) as pseudocapacitive organic materials for EES (Figure 1A). They exhibit a high density of redox-active quinone and imine groups (Figure 1B) and aromatic backbones with extended conjugation. Owing to strong intermolecular hydrogen bonding and donor-acceptor (D-A) π-π interactions, they are insoluble in both organic and aqueous media (Figure 1C). BTABQ and pBTABQ exhibit high charge storage capacities at high charge-discharge rates, which can be associated with rapid pseudocapacitive intercalation processes (Figure 1D). Charge storage and transport occur throughout the electrode bulk, even at practical mass loadings, due to extended electronic delocalization and facile ion transport.

RESULTS AND DISCUSSION

Synthesis and characterization

BTABQ is accessible in gram-quantities by one-step Michael condensation of commercially available tetraamino-*p*-benzoquinone (TABQ) (Figures 1A and S1; Note S1). Although it is highly insoluble in common organic solvents (Figure S2), BTABQ forms as highly crystalline micro-rods (Figures 2A, S3, and S4). The crystal structure of BTABQ was obtained from continuous rotation electron diffraction (cRED) using an *ab initio* method (Figure 2A),[11] following Pawley refinement of the unit cell parameters from the synchrotron powder X-ray diffraction (PXRD) data (Figure S5). High-resolution cRED datasets, down to 0.625 Å, allowed the direct location of all non-hydrogen atoms (Figures S6 and S7; Table S1). BTABQ has a planar, fused tricyclic aromatic backbone with two diaminobenzoquinone moieties bridged by a dihydro-pyrazine core. A closer look at its bond lengths reveals that the two C–NH_2 bonds exhibit a partial double bond character, whereas the two carbonyl bonds exhibit a partial single bond character (Figure 2B), indicating the presence of significant keto-enol tautomerization (Figure 2C). The partial imine character is further verified by the imine carbon chemical shift at 146.4 ppm in the ^{13}C solid-state nuclear magnetic resonance (ssNMR) spectrum (Figure S8), and the C=N stretching band in the Fourier transform infrared (FTIR) spectrum of BTABQ (Figure S9).[12] Each BTABQ molecule engages in hydrogen bonding interactions with six neighboring molecules to form two-dimensional (2D) layers (Figure 2D). The 2D layers stack through short D-A π-π interactions, along the (102) crystallographic direction (Figure S10), to give an interlayer separation of only 3.14 Å (Figures 2E and 2F). The integrity of the 2D layers is maintained on exfoliation, as evidenced by scanning electron microscopy (SEM, Figure S11).

Thermogravimetric analysis and differential scanning calorimetry of BTABQ revealed an endothermic weight loss event around 300°C (Figures S12 and S13). Given the proximity of amino and carbonyl groups in the solid-state structure of BTABQ, we surmised that this process may be associated with further condensation between the neighboring BTABQ molecules. Indeed, heating bulk BTABQ at ~300°C under dynamic vacuum for 2 days yields an amorphous solid with unchanged particle size

[1]Department of Chemistry, Massachusetts Institute of Technology, Cambridge, MA 02139, USA

[2]Berzelii Center EXSELENT on Porous Materials, Department of Materials and Environmental Chemistry, Stockholm University, 10691 Stockholm, Sweden

[3]Department of Fibre and Polymer Technology, KTH Royal Institute of Technology, Teknikringen 56, 10044 Stockholm, Sweden

[4]Center for Functional Nanomaterials, Brookhaven National Laboratory, Upton, NY 11973, USA

[5]Automobili Lamborghini S.p.A., 40019 Sant'Agata Bolognese, Italy

[6]These authors contributed equally

[7]Lead contact

*Correspondence: mdinca@mit.edu

https://doi.org/10.1016/j.joule.2023.03.011

Please cite this article in press as: Chen et al., High-rate, high-capacity electrochemical energy storage in hydrogen-bonded fused aromatics, Joule (2023), https://doi.org/10.1016/j.joule.2023.03.011

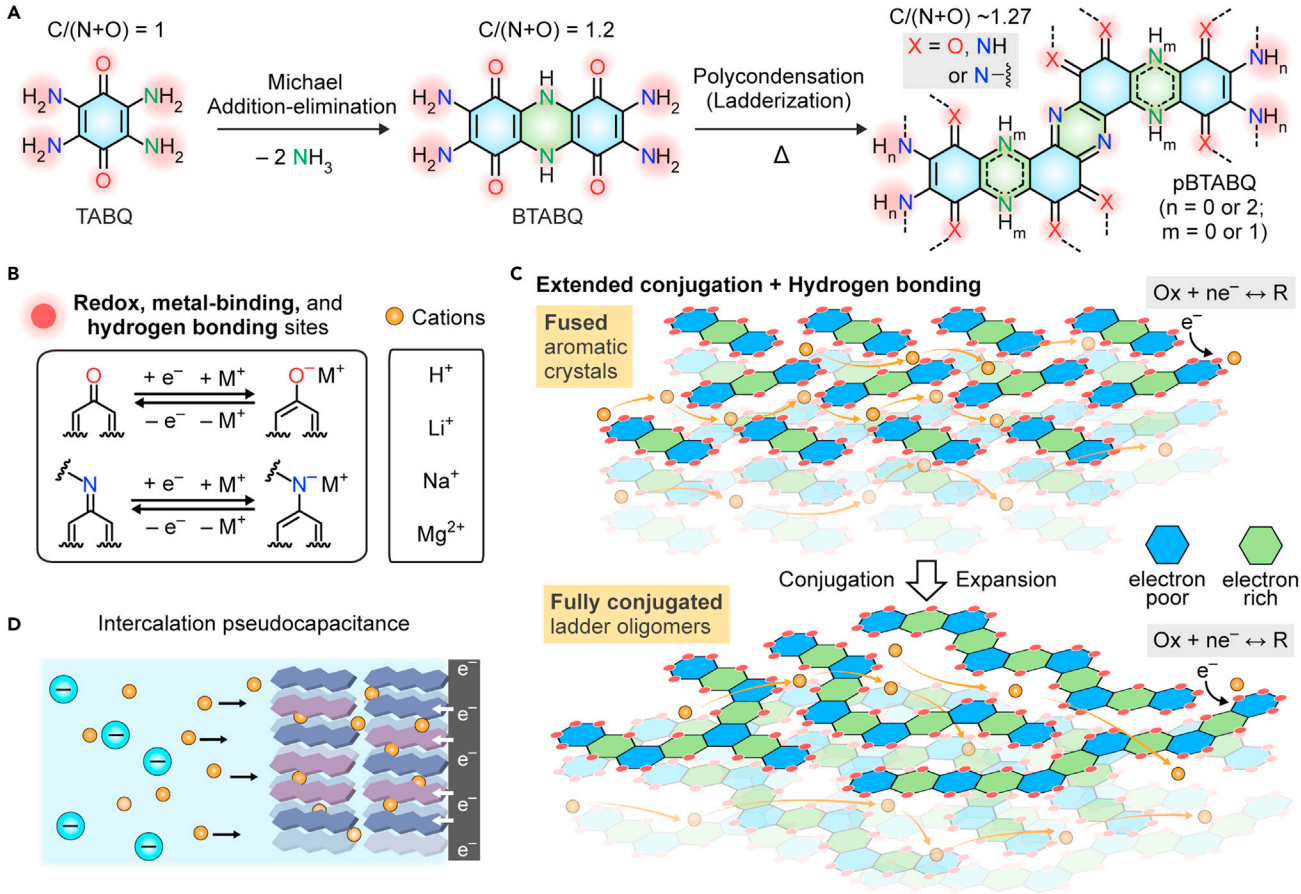

Figure 1. Charge storage in fused aromatic materials

(A) One-step syntheses of BTABQ and pBTABQ.

(B and C) Schematic depiction of fused aromatic molecular crystals and their conversion to conjugated ladder oligomers through self-condensation. The high density of redox-active sites (carbonyl and amine/imine groups) enables an alternating arrangement of electron donor (D) and acceptor (A) moieties. The resulting extended conjugation, strong D-A π-π interactions, and hydrogen bonding facilitate electronic charge delocalization and diffusion of ionic charges.

(D) Representation of pseudocapacitive intercalation of various cations into fused aromatic materials.

and morphology (Figures S14–S16). This solid, termed pBTABQ and accessible in gram-quantities, has a significantly higher molecular weight (Figure S17) and lower oxygen and nitrogen contents than BTABQ (Figure S18; Tables S2 and S3), indicating that ladderization/polymerization of BTABQ with a concomitant loss of water and ammonia (Figure S19) produces a molecular backbone with large extended conjugation.[13] Pair distribution function analyses of both materials reveal similar local structures, confirming that despite the lack of long-range ordering, pBTABQ has a dense solid-state arrangement of molecular fragments analogous to BTABQ (Figure S20). The presence of intermolecular π-π stacking in pBTABQ, itself likely enabled by D-A interactions (Figure S21), was further confirmed by the high-magnification cryo-EM data (Figure S16). Importantly, similar to FTIR spectra, Raman spectroscopy revealed significant resonances between 2,500 and 3,100 cm^{-1} for both BTABQ and pBTABQ, suggesting that the polymer maintains a significant degree of hydrogen bonding (Figure S22). N_2 sorption studies indicate that both materials are non-porous, with similarly low specific surface areas of ~15–20 $m^2\ g^{-1}$ (Figure S23).

Please cite this article in press as: Chen et al., High-rate, high-capacity electrochemical energy storage in hydrogen-bonded fused aromatics, Joule (2023), https://doi.org/10.1016/j.joule.2023.03.011

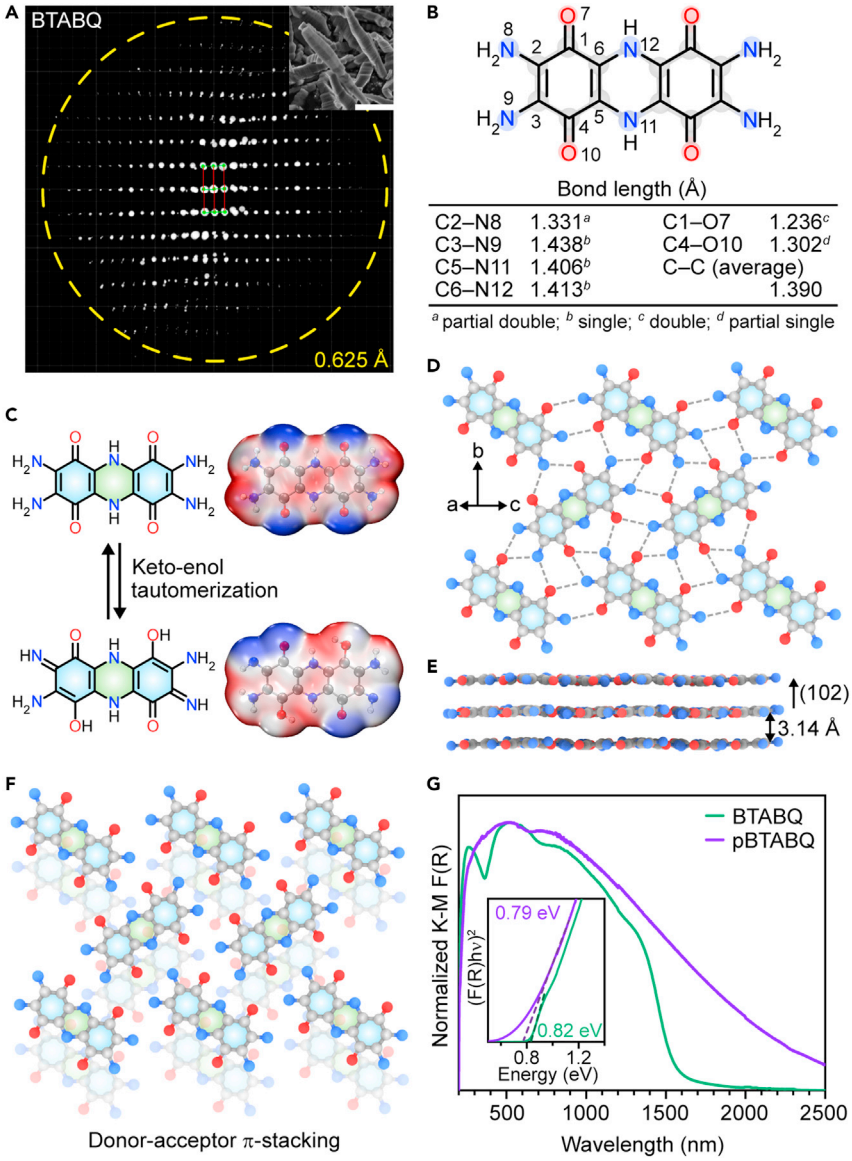

Figure 2. Characterization of BTABQ and pBTABQ

(A) Projection of 3D reciprocal lattice reconstructed from the cRED dataset of BTABQ with a maximum resolution of 0.625 Å. Inset shows a SEM image of BTABQ rods. Scale bar: 2 μm.

(B) Bond lengths in BTABQ.

(C) Keto-enol tautomerization of BTABQ, and the electrostatic potential maps of the two tautomers.

(D) A 2D layer of BTABQ molecules formed by hydrogen bonding interactions (dashed lines) between carbonyl and amine/imine groups. The N···O (2.89 Å) and N···N (3.04 Å) distances are shorter than the sum of their van der Waals radii 3.15 and 3.20 Å, respectively.

(E) π-π stacking of 2D layers of BTABQ with an interlayer distance of 3.14 Å.

(F) D-A alignment of 2D layers.

(G) DRUV-vis-NIR spectra of BTABQ and pBTABQ. Inset shows respective optical band gaps.

Diffuse-reflectance UV-vis (DRUV-vis) spectroscopy revealed that both materials exhibit broad absorption peaks centered around 520 and 800 nm (Figure 2G). The former is typical for π-π^* intra-quinone electronic transitions (Figure S24A), whereas extended conjugation within fused aromatic backbones of BTABQ and pBTABQ accounts for the latter.[14] Although both materials display significant absorptions in the

Please cite this article in press as: Chen et al., High-rate, high-capacity electrochemical energy storage in hydrogen-bonded fused aromatics, Joule (2023), https://doi.org/10.1016/j.joule.2023.03.011

near-infrared region (NIR), leading to narrow optical band gaps of 0.82 and 0.79 eV (Figures 2G and S24D) for BTABQ and pBTABQ, respectively, only the latter has a strong absorption tail into the mid-IR region. This low-energy absorption, rare in organic materials, is indicative of the greater extent of conjugation in pBTABQ relative to BTABQ. Their significant intermolecular electronic delocalization is assisted by strong hydrogen bonding[15] and π-π stacking. Altogether, the various analytical data confirm that pBTABQ is a disordered oligomeric analog of BTABQ that has an extended, fused aromatic backbone, maintains a high density of carbonyl/imine redox sites, and supports a persistent hydrogen bonding network in its solid-state packing (see also Note S2).

BTABQ and pBTABQ exhibit similar bulk electrical conductivities of 2.4×10^{-5} S cm^{-1} ($\bar{\sigma} = 2.33 \times 10^{-5}$ S cm^{-1}) and 0.79×10^{-6} S cm^{-1} ($\bar{\sigma} = 0.40 \times 10^{-6}$ S cm^{-1}) at room temperature, respectively (Figure S25). Despite its larger aromatic backbone, pBTABQ is less conductive than BTABQ likely due to its disordered solid-state packing. Electron paramagnetic resonance spectra exhibit intense isotropic signals that are consistent with the presence of organic radicals in both materials (Figure S26), likely stemming from redox-active quinone/imine moieties or the fused heterocyclic systems within BTABQ units. Overall, the presence of a high density of diverse redox sites in extended conjugated materials with efficient electronic delocalization makes BTABQ and pBTABQ promising candidates for high-rate EES.

Electrochemical performance in neutral electrolytes

Cyclic voltammograms (CVs) of BTABQ and pBTABQ, obtained in a three-electrode configuration in a 1 M aqueous solution of LiCl (see materials and methods), display quasi-rectangular curves at scan rates ranging from 0.2 to 30 mV s^{-1} (Figures 3A and S27). Under cathodic polarization, BTABQ and pBTABQ display stable potential windows of 0.5 and 1.0 V, respectively (Figure S28). An analysis of the CV currents (i) at different scan rates (v) using the power law equation ($i = av^b$) reveals b values close to unity for both materials (Figure 3C), indicating that the charge storage processes are rapid and are not limited by ion diffusion.[16] Altogether, the electrochemical behaviors of BTABQ and pBTABQ diverge from the sharp redox features and the diffusion-limited behaviors (b = 0.5) generally observed for organic battery electrodes[10,17] such as tetraamino-*p*-benzoquinone (TABQ), 5,7,12,14-pentancetetrone (PT) (Figures 3B and 3C), signaling an intrinsically different charge storage mechanism. Significantly, their behavior resembles that reported for inorganic materials such as $RuO_2 \cdot nH_2O$[18,19] and MXenes.[20–22] That is, they behave like capacitors but exhibit a rapid redox-based charge storage mechanism known as pseudocapacitance. Indeed, both BTABQ and pBTABQ have low specific surface areas (<20 m^2 g^{-1}) but exhibit high gravimetric specific capacitances of ~510 F g^{-1} at 0.2 mV s^{-1} and ~300 F g^{-1} at 10 mV s^{-1} (Figure 3D inset), consistent with a pseudocapacitive charge storage mechanism.[23] Notably, BTABQ and pBTABQ deliver these capacitances at high average discharge potentials of 3.21 and 2.96 V vs. Li^+/Li, respectively (Figure 3A). Galvanostatic charge-discharge (GCD) experiments at current densities ranging from 2 to 10 A g^{-1} display triangular (i.e. capacitive) voltage vs. time profiles (Figure S29). In addition, both materials display excellent retention of capacitance over 20,000 CV cycles at a scan rate of 30 mV s^{-1} (Figure 3D). Furthermore, pBTABQ shows ~96% retention in GCD experiments at a current density of 10 A g^{-1} for at least 100,000 cycles (Figure S30). Both materials are stable after long cycling, as verified by XPS of cycled electrodes (Figures S31 and S32). However, BTABQ undergoes *in situ* exfoliation during the first 10 cycles to a stable, crystalline exfoliated microstructure that remains unchanged on subsequent cycling (Figures S33A–S33D, S34A, and S35). By contrast, the morphology and

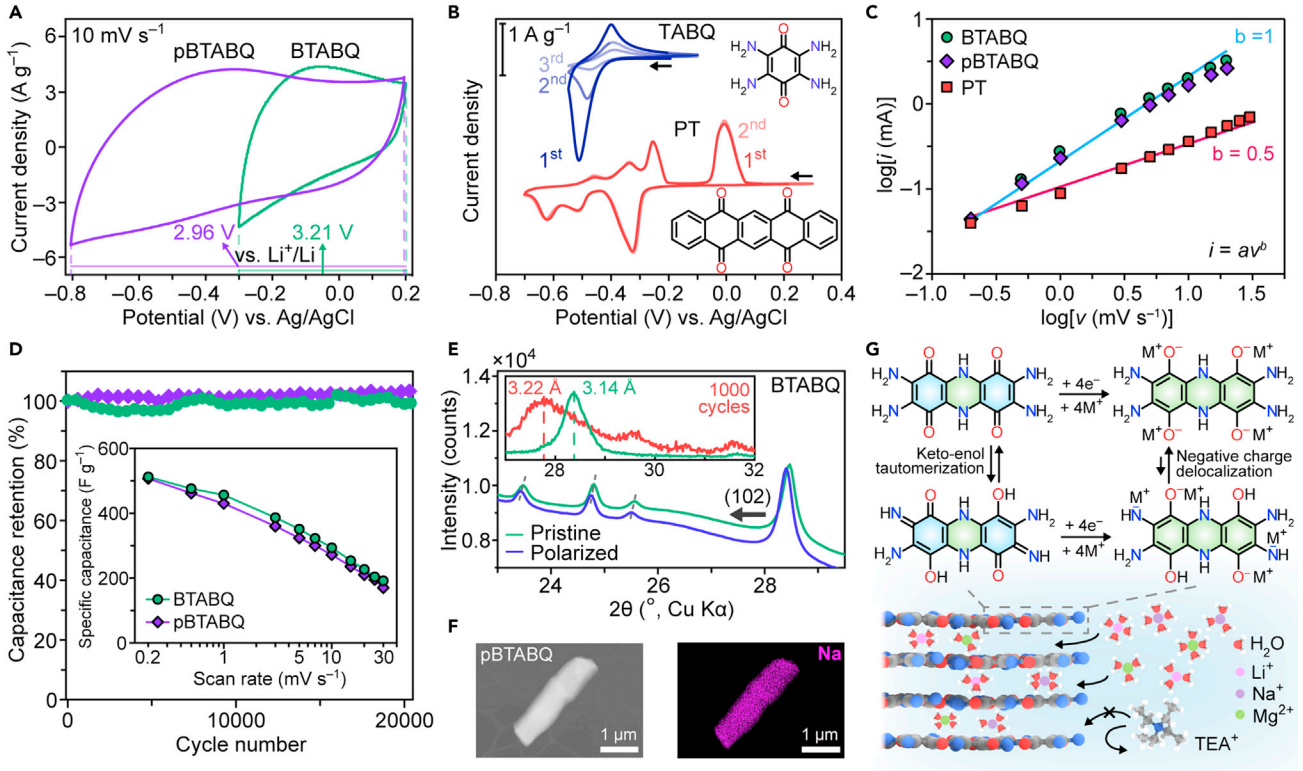

Figure 3. Charge storage in neutral electrolytes

(A) CVs of BTABQ and pBTABQ were obtained at a scan rate of 10 mV s^{-1} using 1 M LiCl aqueous electrolyte. The nominal voltages vs. Li^+/Li are noted for both materials.

(B) CVs of TABQ and PT obtained at a scan rate of 10 mV s^{-1} using 1 M LiCl aqueous electrolyte.

(C) Current versus scan rate analyses of CVs of BTABQ, pBTABQ, and PT using the power law equation.

(D) BTABQ and pBTABQ retain ~98% of their capacitance over 20,000 CV cycles. Inset shows gravimetric specific capacitances at scan rates ranging from 0.2 to 30 mV s^{-1}.

(E) *In situ* WAXS patterns of pristine and negatively polarized BTABQ reveal lattice expansion, indicating intercalation of electrolytic ions under polarization. Inset shows the PXRD patterns of BTABQ electrodes at the pristine stage (green) and after 1,000 cycles (red).

(F) *Ex situ* EDS mapping of pBTABQ shows the presence of Na^+ ions throughout the bulk of a negatively polarized particle.

(G) Schematic representation of redox mechanism of BTABQ and pseudocapacitive intercalation of hydrated ions into BTABQ.

particle size of pBTABQ remain unchanged even after prolonged cycling (Figures S33F–S33H, S34B, and S36).

Electrochemical impedance spectroscopy (EIS) provided additional information on the charge storage behavior under dynamic conditions. Nyquist plots of impedance for both BTABQ and pBTABQ (Figure S37) display typical capacitor-like features with low equivalent series resistances (~1–2 Ω), short semicircles, and 45° transition regions along with an extended 90° capacitive region at low frequencies. Meanwhile, semicircles in the high-frequency region reveal decreasing diameters with applied negative potentials, confirming that fast charge transfer events accompany charge storage in both materials.[24] By contrast, EIS of PT reveals typical battery-like features where charge storage is limited by ion diffusion (Figure S38). Overall, EIS and CVs of BTABQ and pBTABQ display capacitor-like features and highlight a possibility of pseudocapacitive charge storage that is distinct from common organic battery materials.

Redox processes during charge storage were analyzed through *ex situ* X-ray photoelectron spectroscopy (XPS) and ssNMR studies of pristine and negatively polarized

Please cite this article in press as: Chen et al., High-rate, high-capacity electrochemical energy storage in hydrogen-bonded fused aromatics, Joule (2023), https://doi.org/10.1016/j.joule.2023.03.011

electrodes. Deconvolution of O (1s) XPS spectra of polarized electrodes reveal a significant decrease in the intensity of the C=O peak and the appearance of a C–O^- peak, indicating the reduction of carbonyl groups (Figure S39). Deconvolution of N (1s) spectra indicates the disappearance of imine component and the growth of a benzoid-amine component on reduction. The ssNMR spectrum of polarized BTABQ (Figure S40) further supports that both carbonyl and imine groups are reduced and are thus likely responsible for charge storage in BTABQ and pBTABQ (Figure 3G; see also Note S3). Charges stored at these redox sites are delocalized both intramolecularly within the fused aromatic backbones and intermolecularly through hydrogen bonding and D-A π-π stacking, manifesting in distinctly quasi-rectangular CVs, rapid electrode kinetics, and high-rate performance. By contrast, small organic molecules that display intermolecular hydrogen bonding but lack extended conjugation, such as TABQ (Figure S41),[25] and molecules with extensive conjugation but lacking intermolecular hydrogen bonding, such as PT,[26,27] exhibit localized electronic states and display well-defined redox features that are limited by ion diffusion (Figures S24 and S42).[9,10] These comparisons suggest that the combination of all features: fused aromatic backbone with extended conjugation, hydrogen bonding, and π-π stacking are key to pseudocapacitive charge storage in organic materials.

Wide-angle X-ray scattering (WAXS), PXRD, energy-dispersive X-ray spectroscopy (EDS), and angle-resolved XPS (ARXPS) coupled with depth profiling provided insights into whether the pseudocapacitance in BTABQ and pBTABQ is best described as surface-confined or as an intercalation-based bulk process.[5] WAXS patterns for BTABQ electrodes negatively polarized *in situ* display a notable shift of the (102) reflection (Figure 2E) toward a lower 2θ value (Figures 3E, S43, and S44). A PXRD pattern of BTABQ polarized after 1,000 CV cycles revealed a more pronounced shift, corresponding to an increase in interlayer spacing from 3.14 to 3.22 Å during insertion of electrolytic Li^+ ions (Figure 3E inset), and supports an intercalation-based charge storage mechanism. Remarkably, other cations such as Na^+ and Mg^{2+} can also intercalate into both materials, as verified by *ex situ* EDS studies of negatively polarized samples (Figures 3F, S45, and S46). Elemental mapping indicates that a significant amount of metal cations distributes throughout the particles (Table S4), confirming charge storage in the bulk of both BTABQ and pBTABQ electrodes. ARXPS (Figure S47) and XPS depth profiling (Figure S48) for polarized BTABQ and pBTABQ revealed that the amount of metal ions (Li^+ or Na^+) increases with increasing detection depth, confirming that the charge storage occurs via bulk pseudocapacitive intercalation rather than surface confinement.

Studies in a series of different electrolyte solutions provided important information on the role of electrolytic ions on intercalation. Various alkali or alkaline earth metal ions did not cause significant changes in the CVs for both the monomer and the polymer (Figure S49). However, markedly lower currents were observed with electrolytes containing tetraethylammonium (TEA^+) (Figure S50). Partially substituting TEA^+ with increasing amounts of Li^+ led to corresponding increases in current. Altogether, these results show that both materials can intercalate a variety of hydrated alkali and alkaline earth ions but exclude larger TEA^+ ions, presumably based on size (Figure 3G). The ability of BTABQ and pBTABQ to intercalate multiple ions and display size-differentiated pseudocapacitive behavior mimics that of MXenes[20,22] and coordination polymers.[28] Interestingly, the CV shape noted for the BTABQ in tests using Mg^{2+} diverges from a recent report on its use in Zn^{2+} batteries,[17] warranting further focused investigations.

Please cite this article in press as: Chen et al., High-rate, high-capacity electrochemical energy storage in hydrogen-bonded fused aromatics, Joule (2023), https://doi.org/10.1016/j.joule.2023.03.011

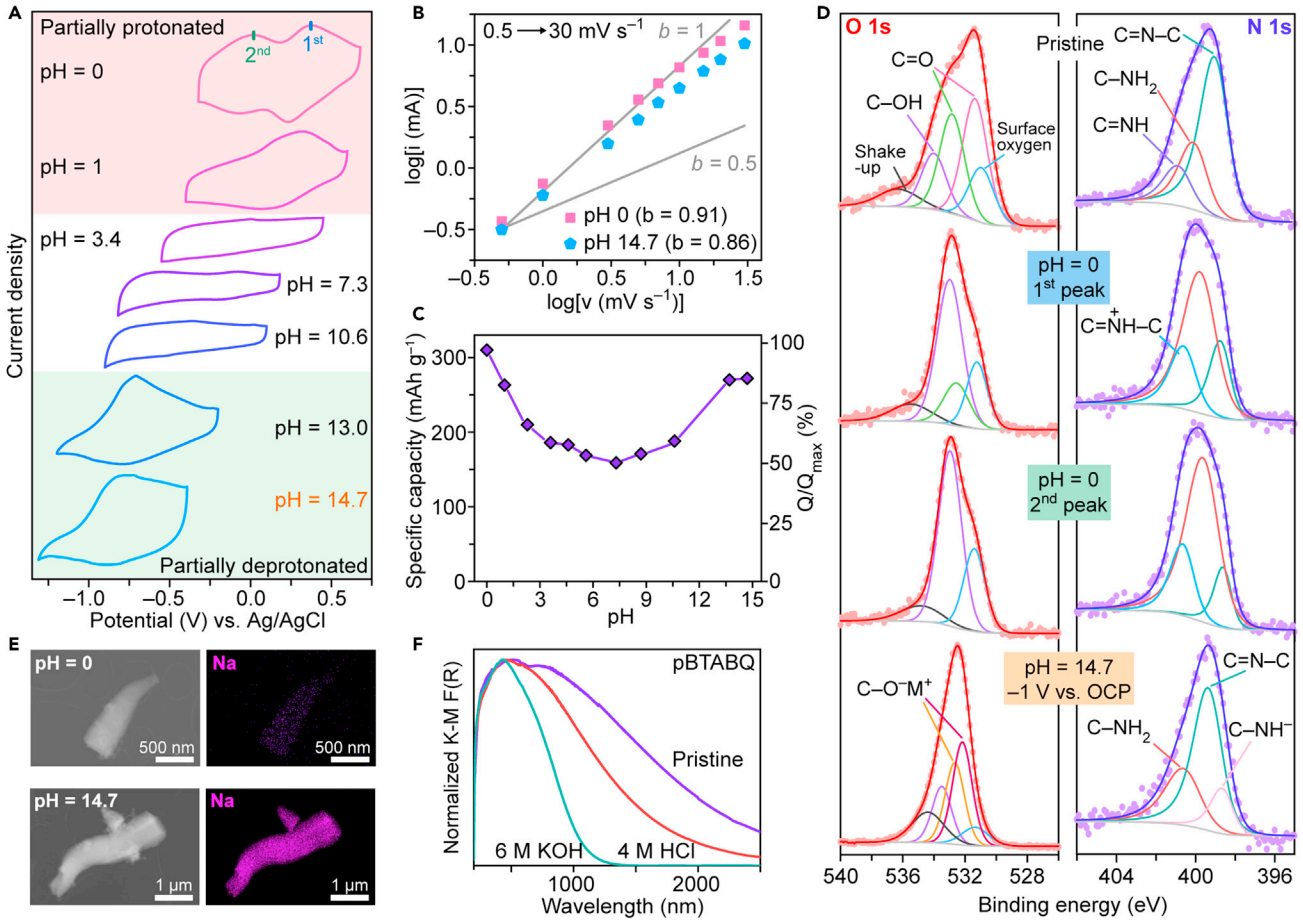

Figure 4. Role of pH on charge storage in pBTABQ

(A) CVs obtained at a scan rate of 5 mV s^{-1} in aqueous 1 M NaCl electrolyte solutions buffered at pH values ranging from 0 to 14.7.

(B) Peak current versus scan rate analyses of the observed peaks under highly acidic and alkaline conditions reveal *b* values close to unity.

(C) Plot of gravimetric specific capacities as a function of electrolyte pH obtained from CVs at a scan rate of 0.2 mV s^{-1}.

(D) *Ex situ* high-resolution O (1s) and N (1s) XPS of polarized electrodes highlight changes at C=O and C=N groups at pH = 0 and 14.7. OCP, open circuit potential.

(E) EDS mappings of polarized pBTABQ at pH = 0 and 14.7.

(F) DRUV-vis spectra of pristine and pBTABQ and after soaking in aqueous solutions of 4 M HCl or 6 M KOH.

Influence of pH on charge storage

The pH of electrolytes often strongly modulates the charge storage behavior of pseudocapacitive materials.[19,29] With evidence in hand that both hydrogen bonding and ion sizes critically influence the electrochemical response of both BTABQ and pBTABQ, we evaluated the influence of pH using aqueous NaCl electrolytes in the pH range 0–14.7 (see supplemental experimental procedures). Although both materials exhibit similar dependence on pH, the discussion below is primarily focused on pBTABQ, given its larger electrochemical stability window (1.0 V).

CVs recorded in electrolytes with intermediate pH (3.0–12.0) remain quasi-rectangular, whereas CVs recorded under highly acidic or alkaline conditions exhibit broad redox features with small peak separations and markedly increased current (Figure 4A). Specifically, two sets of broad redox peaks are noted at pH = 0–1, whereas a single broad redox feature is observed at pH > 13 (Figures S51–S53). The analysis of peak currents vs. scan rates (*vide supra*) finds *b* values of ~0.9 at pH < 1 and

Please cite this article in press as: Chen et al., High-rate, high-capacity electrochemical energy storage in hydrogen-bonded fused aromatics, Joule (2023), https://doi.org/10.1016/j.joule.2023.03.011

pH > 13 (Figure 4B), indicating that even at these pH extremes, charge storage is not limited by bulk ion diffusion. The total amount of charge stored at different pH, calculated as gravimetric specific capacity (mAh g^{-1}) from CVs at 0.2 mV s^{-1}, increases from ~160 mAh g^{-1} at intermediate pHs to 272 and 310 mAh g^{-1} at pH of 14.7 and 0, respectively (Figures 4C and S54). This "U-shaped" pH-dependence of specific capacities has previously been observed for $RuO_2 \cdot xH_2O$[19] but, to our knowledge, is a first in organic systems. The observed capacities are substantially higher than state-of-the-art inorganic pseudocapacitive electrodes and LIC cathodes that function at comparable electrochemical potentials.[5,30] Moreover, high capacities of 225 mAh g^{-1} (pH = 0), 135 mAh g^{-1} (pH = 14.7), and 72 mAh g^{-1} (pH = 7.3) can be accessed at fast rates, within 33 s (Figure S55). pBTABQ exhibits best rate capability at pH = 0, with retentions of 96%, 90%, and 70 % capacities relative to the highest experimental capacity of 320 mAh g^{-1} (Q_{max}, 0.05 mV s^{-1}, Figure S56), at increasing scan rates of 0.2, 5, and 100 mV s^{-1}, respectively (Figure S55). Assuming a minimum of three BTABQ units in every oligomeric pBTABQ unit, one can estimate a 12-electron reduction and a theoretical maximum capacity of 389 mAh g^{-1} for pBTABQ (see Note S3), such that the experimental bulk utility of pBTABQ at pH = 0 is 82%. Remarkably, GCD tests at pH = 0 under high current densities of 2–10 A g^{-1} also deliver capacities greater than 200 mAh g^{-1} at rates corresponding to 6–50 C (1 C = discharge in 1 h), and capacity retention of ~90% after 30,000 cycles (Figure S57). Cycling of pBTABQ at pH = 14 also exhibits ~90% of capacity retention after 10,000 cycles (Figure S58), further demonstrating the chemical and cycling stability of pBTABQ.

Ex situ studies on polarized electrodes provided information on the nature of the redox peaks leading to high capacities under acidic and alkaline conditions. First, a decrease in the intensity of the C=O and C=N components of the O (1s) and N (1s) XPS signals, respectively, on polarization (Figure 4D) suggests that charge storage still occurs through the reduction of imines and carbonyls. A notable difference under highly acidic conditions is the absence of alkaline ions by elemental mapping (Figure 4E) and by XPS (Figure S59), which suggests that protons are exclusively responsible for charge storage under these conditions. Second, the emergence of distinguishable redox peaks suggests that redox states become more localized, likely arising from weakened electronic delocalization through partial protonation or deprotonation of pBTABQ under highly acidic or alkaline conditions. Indeed, soaking pBTABQ in strong acids and bases leads to protonation and deprotonation, respectively, as verified by XPS (Figure S60). Concurrently, the UV-vis spectra show significantly blue-shifted absorption (Figure 4F), as expected for diminished charge delocalization. XPS analysis (Figures 4D and S61) indicates that under acidic conditions, redox processes are proton-assisted, with the first peak involving both imines and carbonyls and the second peak involving only carbonyl moieties. The broad peak observed under alkaline conditions can instead be assigned to the formation of enolates (Figure 4D). The exclusive involvement of protons at the expense of metal cations at high acidity implies excellent bulk proton diffusion under these conditions, as may be expected for Grotthuss transport through the extensive hydrogen-bonding network of pBTABQ (Figure S62).[31] The hydrogen bonding-assisted proton transport may also explain a lack of exfoliation of BTABQ in acidic electrolytes compared with neutral alkali electrolytes (*vide supra*) (Figure S33E). However, the same argument for the role of protons cannot explain the considerable increase in the specific capacity of pBTABQ at pH > 13, where the concentration of protons is very low. Under these conditions, intercalation of hydrated Na^+ dominates, with a substantially larger amount of Na evident by EDS under alkaline conditions than under neutral conditions (Figures 4E, S63, and S64; Table S4). The

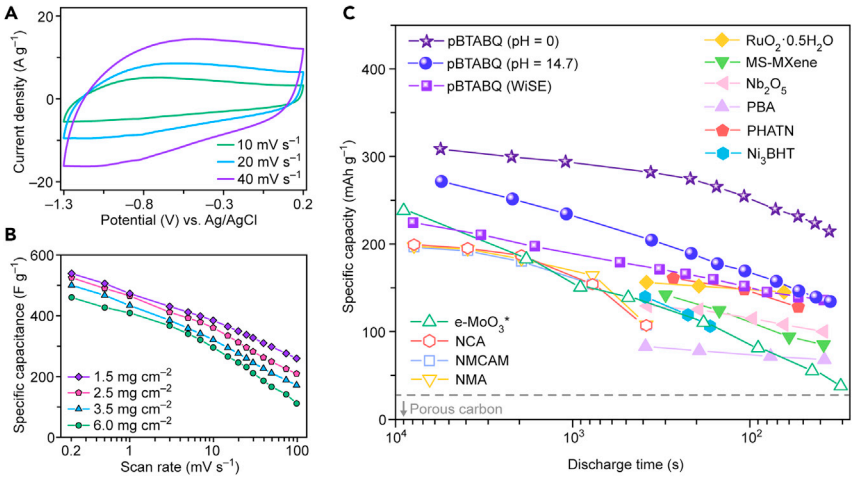

Figure 5. Electrochemical studies in water-in-salt electrolytes (WiSEs) and performance benchmarking

(A) CVs of pBTABQ were obtained at scan rates of 10, 20, and 40 mV s^{-1} using a 17 m $NaClO_4$ WiSE electrolyte.

(B) Power performance of pBTABQ in WiSE obtained from CVs at scan rates ranging from 0.2 to 100 mV s^{-1} on electrodes with active material loadings of 1.5, 2.5, 3.5, and 6.0 mg cm^{-2}.

(C) Comparison of rate performances for pBTABQ and related state-of-the-art LIC cathodes[30,31] or pseudocapacitive[16,21,23,34–36] electrodes. Materials tested at potentials greater than 2 V vs. Li^+/Li and with a minimum active material loading of 1.5 mg cm^{-2} are chosen for comparison. MS-MXene, $Ti_3C_2T_x$ synthesized in molten alkali salts; PBA, Prussian blue analog; PHATN, perylene diimide-hexaazatrinaphthylene; NCA, NMCAM, and NMA, Ni-rich analogs of $LiNiO_2$ doped with Al, Mn, Co, and Mg; Ni_3BHT, Ni_3(benzenehexathiol); e-MoO_3, α-MoO_3 with expanded interlayer gaps, an example of extrinsic pseudocapacitive materials (* mass loading ~0.6 mg cm^{-2}).

seemingly anomalous increase in capacities at the pH extremes highlights the importance of combining intercalation with a flexible hydrogen-bonded structure that either promotes proton transport at low pH or allows deprotonation at high pH, thus allowing metal cation intercalation.[31]

Deep charge-discharge capability

Benefiting from the recent development of water-in-salt electrolytes (WiSEs),[32,33] we explored deep charge-discharge capability of pBTABQ in a larger reductive potential window of 1.5 V. CVs recorded in 17 molal (m) $NaClO_4$ remain quasi-rectangular and deliver capacitances similar to those seen in aqueous neutral electrolytes, with over 90% capacity retention over 40,000 cycles (Figures 5A and S65). The corresponding Nyquist plots recorded under various negative polarizations confirm the capacitor-like features, as with those recorded in aqueous neutral electrolytes (Figure S66). Notably, EDS maps of polarized pBTABQ electrodes in WiSE reveal a significantly larger amount of intercalated Na^+ ions relative to that observed in neutral electrolyte (Figure S67; Table S4). This indeed is reflected in a higher charge capacity of 225 mAh g^{-1} for the WiSE system, a 50% increase relative to neutral aqueous electrolytes. Rate capability studies display ultrahigh-rate performance at various active material loadings as high as 6 mg cm^{-2}, a practical loading value (Figure 5B). For instance, discharge capacities greater than 100 mAh g^{-1} can be delivered within 60 s. A comparison between the performance of pBTABQ in acidic, alkaline, or WiSE electrolytes and state-of-the-art high-capacity LIC cathodes and high-rate pseudocapacitive electrodes is shown in Figure 5C (see also Figure S68). In a full cell, an asymmetric hybrid capacitor fabricated using pBTABQ as the negative electrode and porous-activated carbon as the positive electrode delivers 2 V

Please cite this article in press as: Chen et al., High-rate, high-capacity electrochemical energy storage in hydrogen-bonded fused aromatics, Joule (2023), https://doi.org/10.1016/j.joule.2023.03.011

and cycles safely over 60,000 cycles with a capacitance retention of over 90% (Figures S69 and S70). Optimization of the WiSE electrolyte (see supplemental experimental procedures)[37] further enhances the voltage window to 2.3 V (Figure S71). These preliminary full-cell data and the high average discharge voltage of pBTABQ vs. Li^+/Li (2.71 V, Figure S72) point to future opportunities for further optimizing asymmetric full-cells, for instance by using low voltage anodic materials such as lithium titanium oxide and graphite. Indeed, CVs of pBTABQ in several state-of-the-art WiSE formulations (Figure S73) that function well against lithium titanium oxide and graphite[38] show that our materials retain their performance in these electrochemical environments. Overall, the materials reported here, together with the structural and compositional principles underlining their electrochemical performance, provide important blueprints toward the use of organic pseudocapacitive materials in practical, high-rate, high-capacity EES devices.

EXPERIMENTAL PROCEDURES

Resource availability

Lead contact

Further information and requests for resources and materials should be directed to and will be fulfilled by the lead contact, Mircea Dincă (mdinca@mit.edu).

Materials availability

The materials in this study will be made available upon reasonable request.

Data and code availability

All data are available in the main text and supplemental information, or available from the lead contact on reasonable request. Crystallographic parameters for the structure of BTABQ is archived at the Cambridge Crystallographic Data Center (CCDC) (www.ccdc.cam.ac.uk) under the reference no. CCDC 2144223.

Materials and methods

Synthesis of bis-tetraaminobenzoquinone (BTABQ)

Precursor tetraamino-*p*-benzoquinone (TABQ) is synthesized using a previously reported procedure.[39] To a 15 mL pressure tube (ACE Glass, 150 psi) with 28.4 mg of TABQ and 220 mg of tetrabutylammonium chloride (TBACl, TCI) was added 6 mL of dimethylformamide (DMF, Sigma-Aldrich). The tube was capped under ambient conditions, sonicated for 1 min, and then put into an isothermal oven at 120°C. After 12 h, the tube was cooled down to room temperature, and the reaction mixture was filtered and washed with DMF until the filtrate coming out became colorless. The resulting black solid was further washed with methanol (Sigma-Aldrich) and dried under the air. In total, 15.5 mg of BTABQ was obtained (60% yield). BTABQ is insoluble in common NMR solvents. Solid-state NMR of BTABQ (Figure S8): 174.8 ppm (*C*=O), 146.4 ppm (*C*=N), and 134.5/129.9 ppm (C–N/C–O). Elemental analysis (Table S3): $C_{12}H_{10}O_4N_6$, found: C, 47.14%; H, 2.84%; N, 26.06%; calculated: C, 47.69%; H, 3.33%; N, 27.81%. MALDI-TOF: $[M+H]^+$: found, 302.808; calculated: 303.1; within the $\pm$1 Da error of the instrument (Figure S17). FTIR (cm^{-1}): 3,470, 3,404, 3,356, 3,298, 3,235, 1,651, 1,626, 1,614, 1,568, 1,543, 1,462, 1,364, 1,244, 1,186, 1,136, 721, and 654. The crystallinity of BTABQ was characterized by PXRD (Figure S4). The synthesis of BTABQ can be scaled up to a gram scale. To a 250 mL Schlenk tube (ChemGlass) with 1.07 g of TABQ and 10.3 g of tetrabutylammonium bromide (TBABr, Sigma-Aldrich) was added 80 mL of DMF. The Schlenk tube was sealed under ambient conditions, sonicated for 1 min, and then put into an isothermal oven at 120°C. After 12 h, the Schlenk tube was cooled down to room temperature, and the reaction mixture

was filtered and washed with DMF until the filtrate coming out became colorless. The resulting black solid was further washed with methanol and dried under air yielding 0.4 g of BTABQ (42% yield).

Synthesis of polymerized BTABQ (pBTABQ)

100 mg of BTABQ was transferred into a glass tube, heated at ~300°C under vacuum for 2 days. In total, 85 mg of pBTABQ was obtained as a black solid. Elemental analysis: (Table S3): $C_{36}H_{10}O_{10}N_{16}$, found: C, 52.48%; H, 1.44%; N, 26.34%; calculated: C, 52.31%; H, 1.22%; N, 27.11%. MALDI-TOF: $[M+H]^+$: found, 827.232; calculated: 827.1; $[(M–NH_3)+H]^+$: found, 810.125; calculated: 810.1; within the ±1 Da error of the instrument (Figure S17). The solid-state NMR spectrum of pBTABQ exhibits a broad peak centered at 140 ppm (Figure S8). FTIR (cm^{-1}): 3,468, 3,404, 3,352, 3,298, 3,236, 1,736, 1,686, 1,647, 1,624, 1,543, 1,460, 1,385, 1,358, 1,242, 1,184, 1,134, 1,068, 926, 770, 746, 721, 679, and 633. The synthesis of pBTABQ can be scaled up to a gram scale. However, 1.69 g of BTABQ was added to a 25 mL thick-wall Schlenk tube (Synthware), and the tube was heated at ~300°C under vacuum for 2 days. In total, 1.24 g of pBTABQ was obtained as a black solid.

Electrode and electrolyte preparations

The working electrodes were fabricated as a slurry by mixing active materials, polyvinylidene fluoride (PVDF), and acetylene black carbon in a ratio of 8:1:1 using DMF and were coated onto carbon fiber paper disk (Fuel Cell Earth). The as-prepared electrodes were dried at 65°C in the air for 3 h before drying under the vacuum at 120°C overnight. The dried electrodes have loading densities of 1.5–6 mg cm^{-2}. Approximately, 1.5–2 mg cm^{-2} loading was used for most of the three-electrode cells. 2.5, 3.5, and 6 mg cm^{-2} loadings were used for mass loading-performance studies shown in Figure 5. The activated carbon (YP50) counter electrodes were prepared as thin films by repeated kneading and rolling of a slurry of activated carbon, acetylene black, and a polytetrafluoroethylene (PTFE) solution mixture, in a ratio of 8:1:1, with ethanol. The prepared films were dried at 120°C overnight before use. The BTABQ electrodes for in-house *ex situ* PXRD and solid-state nuclear magnetic resonance (ss-NMR) measurements were also made as thin films using the same method with the same component ratio. 1 M aqueous solutions of LiCl, NaCl, $MgCl_2$, and tetraethylammonium chloride (TEACl) were used for electrochemical tests in neutral conditions. Aqueous electrolytes with pH values ranging from 0 to 14.7, and WiSEs were prepared according to supplemental experimental procedures.

Supercapacitor assembly and electrochemical measurements

The electrode materials were first tested in a three-electrode supercapacitor configuration with porous-activated carbon as counter, a leakless miniature AgCl/Ag (EDAQ, Leakless Miniature AgCl/Ag Reference Electrode, Model ET072) as the reference electrode and a 25 μm thick cellulose sheet as a separator. Porous-activated carbon electrodes with excess weight were used to counter the charges and ensure distinct responses from the working electrodes. A custom-built T-shape Swagelok type cell was used to assemble the cell components.[23] Stainless steel rods are used as current collectors for cells using neutral or basic electrolytes. Titanium rods are used as current collectors for cells using acidic electrolytes. Aqueous solutions of various metal salts were used as electrolytes. Cells were assembled in a fume hood and allowed to rest for 12 h before electrochemical tests. All electrochemical measurements were carried out using a Biologic VSP-300 potentiostat controlled by the software *EC-Lab*. EIS measurements were performed using a multi-sinusoidal signal with an amplitude of 10 mV over a large frequency range of 10 mHz–200

kHz. Stability tests of pBTABQ-based three-electrode cells using WiSEs were performed by holding the potential of pBTABQ electrode at a voltage of −1.3 V (vs. AgCl/Ag) for an hour and measuring impedance (about 15 min). 20 cycles were performed, and equaled to about 30-h potential hold at −1.3 V. Two-electrode asymmetric supercapacitors were fabricated by using BTABQ or pBTABQ electrode as the negative electrode, and porous-activated carbon electrode as the positive electrode, with balanced weight according to their capacitance. The calculations of specific capacitance/capacity and the analysis of electrode kinetics were detailed in supplemental experimental procedures.

Characterizations

PXRD patterns were recorded using a Bruker Advance II diffractometer equipped with a θ/2θ reflection geometry and Ni-filtered Cu Kα radiation ($K\alpha_1$ = 1.5406 Å, $K\alpha_2$ = 1.5444 Å, and $K\alpha_2/K\alpha_1$ = 0.5). The tube voltage and current were 40 kV and 40 mA, respectively. Samples for PXRD were prepared by placing a thin layer of the appropriate material on a zero-background silicon crystal plate. For the *ex situ* measurements of cycled BTABQ electrodes, the thin films were collected from the cycled cells, washed, and dried before being placed at the center of a zero-background silicon crystal plate. High-resolution synchrotron PXRD data were collected at 100 K in the 11-BM beamline at the Advanced Photon Source (APS), Argonne National Laboratory using the Debye-Scherrer geometry and an average calibrated wavelength of 0.458111 Å. Pawley refinement of synchrotron data of BTABQ was conducted using TOPAS Academic (version 6). The refined lattice parameters of BTABQ at 100 K (Figure S5) are a = 4.8923(1) Å, b = 11.2897(3) Å, c = 9.9041(4) Å, β = 101.67° in the space group $P2_1/c$, with R_{wp} = 5.828%, R_{exp} = 5.248%, R_p = 4.667%, and GoF (goodness of fit) = 1.11.

cRED data collection, procession, and structure solution of BTABQ. The crystals were dispersed in ethanol and ultrasonication for 3 min. A droplet of suspension was then transferred to a copper grid with carbon film. The cRED data were collected on a 200 kV JEOL JEM-2100 transmission electron microscope equipped with a quad hybrid pixel detector (Timepix, 512 × 512 pixels, pixel size 55 μm, Amsterdam Sci. Ins.). Before data collection, the sample was cooled down to 96 K by using a Gatan cryo-transfer tomography holder. During data collection, the goniometer was rotated continuously while the selected area electron diffraction (ED) patterns were captured from the crystal simultaneously by using Instamatic software (version 0.6).[40] To balance the intensity of ED and resolution, all the ED patterns were recorded under the spot size 3 with the exposure time 0.5 s. The 3D reciprocal lattice was reconstructed by the software REDp,[41] which was very useful for indexing and obtaining the reflection conditions. For the structure solution of BTABQ, a total of 12 crystals were measured and indexed with monoclinic symmetry, with mean lattice parameters of a = 4.9172(10) Å, b = 11.2565(2) Å, c = 9.9400(2) Å, β = 101.123(3)° in space group of $P2_1/c$ (Figure S6, reflection condition: $h0l, l = 2n$; $00l, l = 2n$; $0k0$, $k = 2n$). The X-ray crystallography software package *XDS* was used for data processing to estimate integrated diffraction intensities.[42] To improve the completeness, *XSCALE* was then applied for data merging,[42] which resulted in a completeness of 99.9% by merging the five datasets. The SHELX software package was used for structural analysis, where SHELXT was used for structure solution.[43] As the resolution of these cRED datasets was measured up to 0.625 Å (Figure S6), all non-hydrogen atomic positions in BTABQ can be located directly by an *ab initio* method. The SHELXL was used for structure refinement using electron scattering factors for all the atoms. The atomic displacement parameters (ADPs) for all framework atoms

were refined anisotropically. Crystallographic details of BTABQ are summarized in Table S1.

ss-NMR spectroscopy was conducted on a three-channel Bruker Avance Neo spectrometer operating at 500.18 MHz and using a 3.2 mm HX solids probe capable of MAS (magic-angle spinning) speeds of up to 24 kHz. The solid samples were packed tightly into 3.2 mm ssNMR zirconia rotors and measured at a MAS speed of 17 kHz. The acquisition time of pristine BTABQ and negatively polarized BTABQ electrode film is about 2 h. The acquisition time of pristine pBTABQ is about 12 h.

XPS measurements were performed using a Physical Electronics PHI VersaProbe II X-ray photoelectron spectrometer equipped with a monochromatic Al anode X-ray source. The main chamber pressure was in the 10^{-10} Torr range. BTABQ and pBTABQ powder samples were pressed on copper tapes with full coverage. *Ex situ* samples were thoroughly washed after cell disassembly and were dried under vacuum before XPS measurements. Survey spectra were collected from 0 to 1,100 eV in binding energy (BE), with a resolution of 0.8 eV. High-resolution spectra of C (1s), N (1s), O (1s), and Li (1s) or Na (1s) (for negatively polarized samples) regions were collected with a resolution of 0.1 eV. BE calibration was not necessary, based on the deconvolution result of the C (1s) region that gives adventitious carbon C1s peak around 284.8 eV. Deconvolution of the C (1s), N (1s), and O (1s) spectra was deconvoluted using CasaXPS. The FWHM of different components of each region were kept similar, except for the shake-up features which are intrinsically broad. Gaussian-Lorentzian product function with 30% of Lorentzian component (GL30) was used for the line shapes during the deconvolution of O (1s). LA(1.5, 2.44, 69) line shape was used for the deconvolution of N (1s) peaks. ARXPS was conducted by tilting the sample stage to realize the change of photoelectron emission angles. Survey and high-resolution spectra of samples were taken at various emission angles, including 20°, 45° (normal XPS mode), 70° and 90°. Depth profiling of samples was conducted using Ar ion sputtering. Each etching cycle takes 60 s. XPS high-resolution scans were conducted after every etching cycle.

DRUV-vis-NIR spectra between 200 and 2,500 nm were collected on a Cary 5000i spectrophotometer, fitted with the UV-vis DiffusIR accessory (Pike Technologies), at the scan rate of 600 nm min^{-1} under ambient conditions. A KBr baseline and a zero-background correction were collected before the sample measurements. Samples were ground in the air with dry KBr (99.9%, Pike technologies) in a mortar and pestle to produce 0.5–1 wt % mixtures.

Room temperature electrical conductivity measurements were carried out at 294 K in an ambient atmosphere on pressed pellets using a 4-probe probe setup described previously.[44] For each sample, the conductivity values were averaged among at least 3 devices.

In situ WAXS measurements were conducted at the Soft Matter Interfaces beamline (12-ID) of the National Synchrotron Light Source II (NSLS-II) at Brookhaven National Laboratory with a beam energy of 16.1 keV and beam size of 200 × 20 μm. The coin cells were connected to the Princeton Applied Research Potentiostat (PARSTAT 2273) for *in situ* bias controlling through metal wires. A homemade 3D printed holder was used to load the coin cell samples on the sample stage for transmission WAXS studies, ensuring that the cells were in the line of the beam (Figure S43). The Scattered data were collected in a vacuum with a PILATUS3 300 kW detector (Dectris, Switzerland), consisting of 0.172 mm square pixels in a 1,475 × 195 array. To obtain

a wide range of wave vector transfer (q), a series of 2D diffraction patterns were collected by rotating the detector on an arc with the sample-to-detector distance being 275 mm. Scattering patterns from each detector angle were stitched together using custom software and then reduced to 1D scattering intensity versus q curve by circular average. *In situ* cells for WAXS were designed by machining commercial CR 2032 Coin cells. Specifically, a hole with a diameter of 3 mm was drilled into the top and bottom casings of the Coin cells. The holes were capped with a piece of Kapton tape and sealed with epoxy to facilitate the transmission of X-rays and prevent electrolytes from leaking. Similar holes were also made in the separator and the porous carbon counter electrode. All cell components were arranged carefully into a stack to ensure seamless transmission of the X-ray beam through the BTABQ pellet. The fabricated cells were tested for their electrochemical performances using cyclic voltammetry before loading them in the WAXS chamber. Cells were tested at their corresponding rest potentials and then reversibly polarized to −0.9 V vs. OCP.

Ex situ high-angle annular dark-field scanning transmission electron microscope (HAADF-STEM) images and energy-dispersive spectroscopy elemental mapping were collected on a JEOL 2010 FEG Analytical Electron Microscope equipped with an Oxford Instrument ULTIM MAX detector. The measurements were conducted while the specimens were under a high vacuum. The specimens were prepared by drop-casting polarized samples onto Cu grids. The specimens were dried under a vacuum overnight before measurements. The negatively polarized samples were thoroughly washed with water to remove any remaining salt before preparing the specimens.

DFT calculations were performed at B3LYP/def2-QZVP level for the two tautomers of BTABQ and at B3LYP/def2-TZVP level for pBTABQ using ORCA. The wave-function analysis was done by Multiwfn.[45,46]

SUPPLEMENTAL INFORMATION

Supplemental information can be found online at https://doi.org/10.1016/j.joule.2023.03.011.

ACKNOWLEDGMENTS

This work was supported by Automobili Lamborghini S.p.A. Part of this work (SEM, XPS, and Raman) made use of the MRSEC Shared Experimental Facilities at MIT, supported by the National Science Foundation under award no. 1419807. The cRED data was collected at the Electron Microscopy Center (EMC), Department of Materials and Environmental Chemistry (MMK) in Stockholm University with the support of the Knut and Alice Wallenberg Foundation (KAW, 2012-0112) through the 3DEM-NATUR project. This research used resources of the Center for Functional Nanomaterials, the SMI beamline (12-ID), and beamline 28-ID-2 (XPD) of the National Synchrotron Light Source II, supported by U.S. DOE Office of Science Facilities at Brookhaven National Laboratory under contract no. DE-SC0012704. Cryo-EM specimens were prepared and imaged at the Automated Cryogenic Electron Microscopy Facility in MIT.nano on a Talos Arctica microscope, a gift from the Arnold and Mabel Beckman Foundation. We thank Dr. Chenyue Sun for help with Raman measurements, Dr. Jianming Bai for help with PDF measurements, Dr. Yong Zhang for help with EDS measurements, Dr. Justin Andrews for help with full-cell fabrication, Julius Oppenheim for help with computational studies, Dr. Ryan McGillicuddy and Prof. Jarad Mason for help with DSC measurements, and Dr. Ruperto Mariano for valuable discussions.

AUTHOR CONTRIBUTIONS

T.C. and M.D. conceived the idea. T.C. designed, synthesized, and characterized BTABQ and pBTABQ. T.C. and H.B. performed and interpreted electrochemistry studies and *in situ* and *ex situ* characterizations. L.Y. performed EPR studies. J.L. conducted the cRED measurements. Y.Z. contributed to the development of the *in situ* WAXS instrumentation, measurements, and data analysis. R.P. contributed to conception and development of the project. T.C. and H.B. wrote the original draft. M.D. reviewed and edited the manuscript. All authors contributed to the interpretation of results and the preparation of manuscript.

DECLARATION OF INTERESTS

M.D., H.B., and T.C. have filed a U.S. Patent (application number PCT/US2022/013925) comprising the work described here.

INCLUSION AND DIVERSITY

We support inclusive, diverse, and equitable conduct of research.

Received: February 16, 2022
Revised: March 17, 2023
Accepted: March 22, 2023
Published: April 17, 2023

REFERENCES

1. Simon, P., and Gogotsi, Y. (2020). Perspectives for electrochemical capacitors and related devices. Nat. Mater. *19*, 1151–1163. https://doi.org/10.1038/s41563-020-0747-z.

2. Gür, T.M. (2018). Review of electrical energy storage technologies, materials and systems: challenges and prospects for large-scale grid storage. Energy Environ. Sci. *11*, 2696–2767. https://doi.org/10.1039/C8EE01419A.

3. Simon, P., Gogotsi, Y., and Dunn, B. (2014). Materials science. Where do batteries end and supercapacitors begin? Science *343*, 1210–1211. https://doi.org/10.1126/science.1249625.

4. Zou, Z., Xu, J., Zeng, F., and Mei, X. (2019). A hybrid energy storage system for dual-motor driven electric vehicles. DEStech Trans. Environ. Energy Earth Sci. 145–148.

5. Choi, C., Ashby, D.S., Butts, D.M., DeBlock, R.H., Wei, Q., Lau, J., and Dunn, B. (2020). Achieving high energy density and high power density with pseudocapacitive materials. Nat. Rev. Mater. *5*, 5–19. https://doi.org/10.1038/s41578-019-0142-z.

6. Fleischmann, S., Mitchell, J.B., Wang, R., Zhan, C., Jiang, D.E., Presser, V., and Augustyn, V. (2020). Pseudocapacitance: from fundamental understanding to high power energy storage materials. Chem. Rev. *120*, 6738–6782. https://doi.org/10.1021/acs.chemrev.0c00170.

7. Sun, H., Mei, L., Liang, J., Zhao, Z., Lee, C., Fei, H., Ding, M., Lau, J., Li, M., Wang, C., et al. (2017). Three-dimensional holey-graphene/niobia composite architectures for ultrahigh-rate energy storage. Science *356*, 599–604. https://doi.org/10.1126/science.aam5852.

8. Xia, Y., Mathis, T.S., Zhao, M.Q., Anasori, B., Dang, A., Zhou, Z., Cho, H., Gogotsi, Y., and Yang, S. (2018). Thickness-independent capacitance of vertically aligned liquid-crystalline MXenes. Nature *557*, 409–412. https://doi.org/10.1038/s41586-018-0109-z.

9. Poizot, P., Gaubicher, J., Renault, S., Dubois, L., Liang, Y., and Yao, Y. (2020). Opportunities and challenges for organic electrodes in electrochemical energy storage. Chem. Rev. *120*, 6490–6557. https://doi.org/10.1021/acs.chemrev.9b00482.

10. Lu, Y., Zhang, Q., Li, L., Niu, Z., and Chen, J. (2018). Design strategies toward enhancing the performance of organic electrode materials in metal-ion batteries. Chem *4*, 2786–2813. https://doi.org/10.1016/j.chempr.2018.09.005.

11. Huang, Z., Grape, E.S., Li, J., Inge, A.K., and Zou, X. (2021). 3D electron diffraction as an important technique for structure elucidation of metal-organic frameworks and covalent organic frameworks. Coord. Chem. Rev. *427*, 213583. https://doi.org/10.1016/j.ccr.2020.213583.

12. Waller, P.J., Lyle, S.J., Osborn Popp, T.M., Diercks, C.S., Reimer, J.A., and Yaghi, O.M. (2016). Chemical conversion of linkages in covalent organic frameworks. J. Am. Chem. Soc. *138*, 15519–15522. https://doi.org/10.1021/jacs.6b08377.

13. Lee, J., Kalin, A.J., Yuan, T., Al-Hashimi, M., and Fang, L. (2017). Fully conjugated ladder polymers. Chem. Sci. *8*, 2503–2521. https://doi.org/10.1039/C7SC00154A.

14. Audi, H., Chen, Z., Charaf-Eddin, A., D'Aléo, A., Canard, G., Jacquemin, D., and Siri, O. (2014). Extendable nickel complex tapes that reach NIR absorptions. Chem. Commun. (Camb) *50*, 15140–15143. https://doi.org/10.1039/C4CC07353C.

15. Isono, T., Kamo, H., Ueda, A., Takahashi, K., Nakao, A., Kumai, R., Nakao, H., Kobayashi, K., Murakami, Y., and Mori, H. (2013). Hydrogen bond-promoted metallic state in a purely organic single-component conductor under pressure. Nat. Commun. *4*, 1344. https://doi.org/10.1038/ncomms2352.

16. Augustyn, V., Come, J., Lowe, M.A., Kim, J.W., Taberna, P.L., Tolbert, S.H., Abruña, H.D., Simon, P., and Dunn, B. (2013). High-rate electrochemical energy storage through Li^+ intercalation pseudocapacitance. Nat. Mater. *12*, 518–522. https://doi.org/10.1038/nmat3601.

17. Lin, L., Lin, Z., Zhu, J., Wang, K., Wu, W., Qiu, T., and Sun, X. (2023). A semi-conductive organic cathode material enabled by extended conjugation for rechargeable aqueous zinc batteries. Energy Environ. Sci. *16*, 89–96. https://doi.org/10.1039/D2EE02961H.

18. Zheng, J.P., Cygan, P.J., and Jow, T.R. (1995). Hydrous ruthenium oxide as an electrode material for electrochemical capacitors. J. Electrochem. Soc. *142*, 2699–2703. https://doi.org/10.1149/1.2050077.

19. Burke, L.D., Murphy, O.J., O'Neill, J.F., and Venkatesan, S. (1977). The oxygen electrode. Part 8.—oxygen evolution at ruthenium dioxide anodes. J. Chem. Soc. Faraday Trans. 1 *73*, 1659–1671. https://doi.org/10.1039/F19777301659.

20. Lukatskaya, M.R., Mashtalir, O., Ren, C.E., Dall'Agnese, Y., Rozier, P., Taberna, P.L., Naguib, M., Simon, P., Barsoum, M.W., and Gogotsi, Y. (2013). Cation intercalation and high volumetric capacitance of

two-dimensional titanium carbide. Science *341*, 1502–1505. https://doi.org/10.1126/science.1241488.

21. Li, Y., Shao, H., Lin, Z., Lu, J., Liu, L., Duployer, B., Persson, P.O.Å., Eklund, P., Hultman, L., Li, M., et al. (2020). A general Lewis acidic etching route for preparing MXenes with enhanced electrochemical performance in non-aqueous electrolyte. Nat. Mater. *19*, 894–899. https://doi.org/10.1038/s41563-020-0657-0.

22. Wang, X., Mathis, T.S., Li, K., Lin, Z., Vlcek, L., Torita, T., Osti, N.C., Hatter, C., Urbankowski, P., Sarycheva, A., et al. (2019). Influences from solvents on charge storage in titanium carbide MXenes. Nat. Energy *4*, 241–248. https://doi.org/10.1038/s41560-019-0339-9.

23. Banda, H., Dou, J.H., Chen, T., Libretto, N.J., Chaudhary, M., Bernard, G.M., Miller, J.T., Michaelis, V.K., and Dincă, M. (2021). High-capacitance pseudocapacitors from Li^+ ion intercalation in nonporous, electrically conductive 2D coordination polymers. J. Am. Chem. Soc. *143*, 2285–2292. https://doi.org/10.1021/jacs.0c10849.

24. Mathis, T.S., Kurra, N., Wang, X., Pinto, D., Simon, P., and Gogotsi, Y. (2019). Energy storage data reporting in perspective—guidelines for interpreting the performance of electrochemical energy storage systems. Adv. Energy Mater. *9*, 1902007. https://doi.org/10.1002/aenm.201902007.

25. Lin, Z., Shi, H.Y., Lin, L., Yang, X., Wu, W., and Sun, X. (2021). A high capacity small molecule quinone cathode for rechargeable aqueous zinc-organic batteries. Nat. Commun. *12*, 4424. https://doi.org/10.1038/s41467-021-24701-9.

26. Han, C., Li, H., Li, Y., Zhu, J., and Zhi, C. (2021). Proton-assisted calcium-ion storage in aromatic organic molecular crystal with coplanar stacked structure. Nat. Commun. *12*, 2400. https://doi.org/10.1038/s41467-021-22698-9.

27. Wang, C., Jiang, C., Xu, Y., Liang, L., Zhou, M., Jiang, J., Singh, S., Zhao, H., Schober, A., and Lei, Y. (2016). A selectively permeable membrane for enhancing cyclability of organic sodium-ion batteries. Adv. Mater. *28*, 9182–9187. https://doi.org/10.1002/adma.201603240.

28. Banda, H., Dou, J.H., Chen, T., Zhang, Y., and Dincă, M. (2021). Dual-ion intercalation and high volumetric capacitance in a two-dimensional non-porous coordination polymer. Angew. Chem. Int. Ed. Engl. *60*, 27119–27125. https://doi.org/10.1002/anie.202112811.

29. Wen, S., Lee, J.W., Yeo, I.H., Park, J., and Mho, S.I. (2004). The role of cations of the electrolyte for the pseudocapacitive behavior of metal oxide electrodes, MnO_2 and RuO_2. Electrochim. Acta *50*, 849–855. https://doi.org/10.1016/j.electacta.2004.02.056.

30. Li, W., Lee, S., and Manthiram, A. (2020). High-nickel NMA: a cobalt-free alternative to NMC and NCA cathodes for lithium-ion batteries. Adv. Mater. *32*, e2002718. https://doi.org/10.1002/adma.202002718.

31. Wu, X., Hong, J.J., Shin, W., Ma, L., Liu, T., Bi, X., Yuan, Y., Qi, Y., Surta, T.W., Huang, W., et al. (2019). Diffusion-free Grotthuss topochemistry for high-rate and long-life proton batteries. Nat. Energy *4*, 123–130. https://doi.org/10.1038/s41560-018-0309-7.

32. Suo, L., Borodin, O., Gao, T., Olguin, M., Ho, J., Fan, X., Luo, C., Wang, C., and Xu, K. (2015). "Water-in-salt" electrolyte enables high-voltage aqueous lithium-ion chemistries. Science *350*, 938–943. https://doi.org/10.1126/science.aab1595.

33. Chao, D., and Qiao, S.Z. (2020). Toward high-voltage aqueous batteries: super- or low-concentrated electrolyte? Joule *4*, 1846–1851. https://doi.org/10.1016/j.joule.2020.07.023.

34. Russell, J.C., Posey, V.A., Gray, J., May, R., Reed, D.A., Zhang, H., Marbella, L.E., Steigerwald, M.L., Yang, Y., Roy, X., et al. (2021). High-performance organic pseudocapacitors via molecular contortion. Nat. Mater. *20*, 1136–1141. https://doi.org/10.1038/s41563-021-00954-z.

35. Ma, H., Kong, D., Xu, Y., Xie, X., Tao, Y., Xiao, Z., Lv, W., Jang, H.D., Huang, J., and Yang, Q.H. (2017). Disassembly–reassembly approach to RuO_2/graphene composites for ultrahigh volumetric capacitance supercapacitor. Small *13*, 1701026. https://doi.org/10.1002/smll.201701026.

36. Yu, M., Shao, H., Wang, G., Yang, F., Liang, C., Rozier, P., Wang, C.Z., Lu, X., Simon, P., and Feng, X. (2020). Interlayer gap widened α-phase molybdenum trioxide as high-rate anodes for dual-ion-intercalation energy storage devices. Nat. Commun. *11*, 1348. https://doi.org/10.1038/s41467-020-15216-w.

37. Jaumaux, P., Yang, X., Zhang, B., Safaei, J., Tang, X., Zhou, D., Wang, C., and Wang, G. (2021). Localized water-in-salt electrolyte for aqueous lithium-ion batteries. Angew. Chem. Int. Ed. Engl. *60*, 19965–19973. https://doi.org/10.1002/anie.202107389.

38. Yang, C., Chen, J., Qing, T., Fan, X., Sun, W., Von Cresce, A., Ding, M.S., Borodin, O., Vatamanu, J., Schroeder, M.A., et al. (2017). 4.0 V aqueous Li-ion batteries. Joule *1*, 122–132. https://doi.org/10.1016/j.joule.2017.08.009.

39. Chen, T., Dou, J.H., Yang, L., Sun, C., Oppenheim, J.J., Li, J., and Dincă, M. (2022). Dimensionality modulates electrical conductivity in compositionally constant one-, two-, and three-dimensional frameworks. J. Am. Chem. Soc. *144*, 5583–5593. https://doi.org/10.1021/jacs.2c00614.

40. Smeets, S., Wang, B., Cichocka, M.O., Angstrom, J., and Wan, W. (2018). Instamatic (Version 0.6). Zenodo. https://doi.org/10.5281/zenodo.1217026.

41. Wan, W., Sun, J., Su, J., Hovmöller, S., and Zou, X. (2013). Three-dimensional rotation electron diffraction: software RED for automated data collection and data processing. J. Appl. Crystallogr. *46*, 1863–1873. https://doi.org/10.1107/S0021889813027714.

42. Kabsch, W. (2010). Integration, scaling, space-group assignment and post-refinement. Acta Crystallogr. D Biol. Crystallogr. *66*, 133–144. https://doi.org/10.1107/S0907444909047374.

43. Sheldrick, G.M. (2008). A short history of SHELX. Acta Crystallogr. A *64*, 112–122. https://doi.org/10.1107/S0108767307043930.

44. Sun, L., Park, S.S., Sheberla, D., and Dincă, M. (2016). Measuring and reporting electrical conductivity in metal−organic frameworks: Cd_2(TTFTB) as a case study. J. Am. Chem. Soc. *138*, 14772–14782. https://doi.org/10.1021/jacs.6b09345.

45. Lu, T., and Chen, F. (2012). Multiwfn: a multifunctional wavefunction analyzer. J. Comput. Chem. *33*, 580–592. https://doi.org/10.1002/jcc.22885.

46. Zhang, J., and Lu, T. (2021). Efficient evaluation of electrostatic potential with computerized optimized code. Phys. Chem. Chem. Phys. *23*, 20323–20328. https://doi.org/10.1039/D1CP02805G.